# Source Estimates for MEG/EEG Visual Evoked Responses Constrained by Multiple, Retinotopically-Mapped Stimulus Locations

**Donald J. Hagler Jr.,**[1,2]* **Eric Halgren,**[1,2,3,4] **Antigona Martinez,**[3,5] **Mingxiong Huang,**[2] **Steven A. Hillyard,**[3] **and Anders M. Dale**[1,2,3]

[1]*Multimodal Imaging Laboratory, University of California, San Diego*
[2]*Department of Radiology, University of California, San Diego*
[3]*Department of Neurosciences, University of California, San Diego*
[4]*Department of Psychiatry, University of California, San Diego*
[5]*Nathan Kline Institute, New York University, New York*

◆ ══════════════════ ◆

**Abstract:** Studying the human visual system with high temporal resolution is a significant challenge due to the limitations of the available, noninvasive measurement tools. MEG and EEG provide the millisecond temporal resolution necessary for answering questions about intracortical communication involved in visual processing, but source estimation is ill-posed and unreliable when multiple; simultaneously active areas are located close together. To address this problem, we have developed a retinotopy-constrained source estimation method to calculate the time courses of activation in multiple visual areas. Source estimation was disambiguated by: (1) fixing MEG/EEG generator locations and orientations based on fMRI retinotopy and surface tessellations constructed from high-resolution MRI images; and (2) solving for many visual field locations simultaneously in MEG/EEG responses, assuming source current amplitudes to be constant or varying smoothly across the visual field. Because of these constraints on the solutions, estimated source waveforms become less sensitive to sensor noise or random errors in the specification of the retinotopic dipole models. We demonstrate the feasibility of this method and discuss future applications such as studying the timing of attentional modulation in individual visual areas. *Hum Brain Mapp 30:1290–1309, 2009.* © **2008 Wiley-Liss, Inc.**

**Key words:** visual evoked response; retinotopy; inverse; MEG; EEG; fMRI

◆ ══════════════════ ◆

## INTRODUCTION

The primate visual system is a densely interconnected, hierarchical network comprising retinal photoreceptors,

subcortical relays, multiple visual cortical areas, and higher-level areas necessary for functions such as memory, emotion, and attention [Bullier and Nowak, 1995; Colby and Goldberg, 1999; Felleman and Van Essen, 1991; Kastner and Ungerleider, 2000]. Invasive studies of non-human primates have provided much of our understanding about how the various visual areas are interconnected and functionally different from each other [Felleman and Van Essen, 1991; Sereno and Allman, 1991]. In humans, fMRI has proven to be a useful tool for identifying the map boundaries in human visual cortex [DeYoe et al., 1996; Engel et al., 1994; Sereno et al., 1995], leading to studies of the different stimulus preferences of individual visual areas [Avidan et al., 2002; Gardner et al., 2005; Seiffert

et al., 2003; Singh et al., 2000; Tootell et al., 1995, 1997, 1998b]. This method has also enabled measurement of attentional modulation in individual visual areas, demonstrating increased activation with selective attention in V1 and other visual areas [Brefczynski and DeYoe, 1999; Gandhi et al., 1999; Martinez et al., 1999; Noesselt et al., 2002; Sasaki et al., 2001; Slotnick et al., 2003; Somers et al., 1999; Tootell et al., 1998a]. Recently, multiple maps have been observed in the higher-level areas involved in attentional control, including posterior parietal cortex (PPC), frontal eye fields (FEF), and dorsolateral prefrontal cortex (DLFPC) [Hagler and Sereno, 2006; Hagler et al., 2007; Kastner et al., 2007; Schluppeck et al., 2005; Sereno et al., 2001; Silver et al., 2005; Swisher et al., 2007]. FMRI has provided some insight into how stimulus or task conditions result in differential recruitment of these higher-level maps, but temporal correlations between these maps remain unexplored.

Noninvasively studying interactions within this complicated array of brain areas is made difficult by the limited temporal or spatial resolution of currently available brain imaging methods. Because of its low temporal resolution, fMRI is not well suited for studying the time course of activation in visual areas. Magnetoencephalography (MEG) and electroencephalography (EEG) measure magnetic fields and electrical potentials with millisecond temporal resolution, but methods to localize the sources of those fields and potentials have limited spatial resolution [Dale and Halgren, 2001; Hamalainen et al., 1993]. Methods combining these brain imaging techniques have been developed in the past [Dale and Sereno, 1993; Dale et al., 2000; Di Russo et al., 2005; Vanni et al., 2004], but their successful application to the study of the early visual areas has been somewhat limited.

The difficulty in MEG/EEG source estimation (i.e., the inverse problem) is that, given a large number of dipoles distributed throughout the brain, the number of possible combinations of those dipoles that can result in a particular distribution of sensor amplitudes is infinite. Even a small number of dipoles, if allowed to rotate freely and vary in amplitude, can produce a wide variety of sensor amplitude distributions. Some combinations of dipoles may be more physiologically likely than others, but additional information is required to make such determinations [Dale and Sereno, 1993; Dale and Halgren, 2001; Dale et al., 2000; Hamalainen et al., 1993]. For example, structural MRI data can be used to force the dipoles to be located in the gray matter of the cerebral cortex. Furthermore, because the dendrites of pyramidal neurons, which are primarily responsible for generating MEG and EEG signals, run across the cortical layers, the orientation of each current dipole can be assumed to be perpendicular to the cortical sheet. In addition, fMRI data can be used to further bias the source estimates; either as an initial guess or hard localization constraint in equivalent current dipole (ECD) modeling [Di Russo et al., 2005; Vanni et al., 2004], or as a Bayesian prior in distributed source estimation

methods [Dale and Sereno, 1993; Dale et al., 2000; Liu et al., 1998; Schmidt et al., 1999].

The minimum-norm inverse method estimates distributed sources and requires no *a priori* assumptions about the locations or number of sources, but the solution space can be limited to the cortical surface and biased with fMRI data [Dale and Sereno, 1993; Dale et al., 2000; Liu et al. 1998]. Minimum-norm estimates for visual evoked responses (VERs) have shown a rough correspondence with the retinotopic organization of primary visual cortex, but time courses for individual visual areas such as V1 and V2 have not been demonstrated with this method [Ahlfors et al., 1992; Sharon et al., 2007]. ECD modeling is a common method for MEG and EEG source estimation that has been used in several studies to model the generators of visual evoked fields and potentials (VEFs and VEPs). The method involves iteratively searching for a dipole model that results in a least-squares best-fit [Scherg, 1990; Supek and Aine, 1993]. Several studies have localized dipoles with properties consistent with the retinotopic layout of primary visual cortex [Aine et al., 1996; Clark et al., 1995; Jeffreys and Axford, 1972; Slotnick et al., 1999]. More recent studies have extended those results, modeling the time course of the VEP with a larger number of dipoles [Di Russo et al., 2001, 2003, 2005; Martinez et al., 2001; Vanni et al., 2004]. Vanni et al. and Di Russo et al. used fMRI data to fix dipole locations in multiple visual areas [Di Russo et al., 2005; Vanni et al., 2004], although for practical and methodological reasons, single dipoles were made to model the activity of multiple visual areas (e.g. V2, V3, and V3A).

These studies have highlighted how difficult it is to resolve the time courses of activity in individual visual areas, primarily because of their close proximity. Even if fitted dipoles are constrained by fMRI data, crosstalk between the dipoles prevents meaningful separation of the signals [Liu et al., 1998; Sereno, 1998; Vanni et al., 2004]. The similarity in position and orientation of these dipoles results in fundamental ambiguity that cannot be resolved without additional information. Slotnick et al. integrated data from multiple stimulus locations with an iso-eccentricity temporal constraint [Slotnick et al., 1999], and in the present study we used a variation of this method to resolve those ambiguities and determine the time courses of individual visual areas. We created detailed models of dipoles in multiple visual areas, with their cortical locations and orientations varying as functions of stimulus location in an iso-eccentricity band of the visual field. Source strengths for a given visual area were constrained to be equal, or at least smoothly varying, as a function of stimulus location. Because the VEPs/VEFs were fitted with dipole paths along distinctively folded patches of cortex for each visual area, rather than a single dipole in each visual area, much of the ambiguity, and thus crosstalk between visual areas, was eliminated.

This retinotopy-constrained inverse method that we have developed allows the measurement of time courses

of activation of multiple visual areas. This method resolves the inherent ambiguity due to the close proximity and simultaneous activation of these areas. This in turn will allow for the measurement of differences in activation—whether related to stimulus properties, attentional state, cognitive task requirements, brain disorder, or all of the above—across time, with millisecond accuracy, in individual visual areas and the comparison of those differences to the time courses of activation in higher-level cortical areas involved in executive control. This provides a promising new approach for the noninvasive measurement of cortico–cortical interactions and analysis of neurocognitive information processing.

## METHODS

### Participants

Two female adults participated in this study (ages 19 and 21). The experimental protocol was approved by the UCSD institutional review board, and informed consent was obtained from both participants. Both subjects were right handed and had normal or corrected to normal vision. One of the subjects ("Subject 1") was used to develop and test the retinotopy-constrained inverse methods in detail. Data for a second subject ("Subject 2") is included for comparison.

### Stimulus Presentation and Behavioral Monitoring

For fMRI sessions, stimuli were presented via a mirror reflection of a plastic screen placed inside the bore of the magnet, and a standard video projector with a custom zoom lens was used to project images onto this screen from a distance. For MEG/EEG sessions, visual stimuli were presented with a three mirror DLP projector. An MRI-compatible fiber-optical button box was used for fMRI experiments requiring subject responses; for MEG/EEG sessions, a finger lifting response was used with a laser and light sensor device. Dental impression bitebars to immobilize the top row of teeth were used for fMRI sessions. Subjects' heads were supported and surrounded by foam padding. To ensure that the eccentricity of stimuli matched for fMRI and MEG/EEG sessions, the distance between the subject's nasion and the screen was measured and the zoom of the projector lens adjusted to achieve a maximum visual angle of ∼20° (top to bottom of displayable area).

### Simultaneous MEG/EEG Measurement

MEG and EEG are in some ways complementary, making it useful to acquire data with both modalities [Dale and Sereno, 1993; Liu et al., 2002; Sharon et al., 2007]. MEG signals were measured with an Elekta/Neuromag Vectorview 306 channel whole head neuromagnetometer, which comprises two planar gradiometers and one magne-

tometer at each of 102 locations. EEG signals were simultaneously measured with a non-magnetic 60-channel electrode cap. Two additional electrodes were used to monitor eye blinks and movements. The sampling frequency for the MEG-EEG recording was 1,000 Hz with an anti-aliasing low-pass filter of 333 Hz. Data were band-pass filtered offline between 0.2 and 50 Hz. The locations of sensors with respect to landmarks on the head were measured using a Polhemus FastTrack 3-D digitizer. After rejecting trials containing artifacts such as eye blinks, data from all trials were used to calculate average time series as well as a noise covariance matrix, which represents the contribution of random noise to the signals measured at each of the detectors. MEG and EEG data were averaged across trials time-locked to stimulus onset.

Combined MEG and EEG were used to measure evoked responses to small visual stimuli consisting of circular patches (1.5° in diameter) with a two-dimensional, grayscale sine grating, forming a type of checkerboard (see Fig. 2). Stimuli were presented on a gray background at maximum contrast. The sine gratings had a spatial frequency of four cycles/degree of visual angle. Stimuli were briefly (87 ms) presented at one of 16 polar angles at an eccentricity of 5° of visual angle. To ensure that subjects maintained a stable level of alertness and maintained central fixation, subjects were given a simple task in which they made a button press upon rare dimming of the central fixation cross. The interval between successive stimulus onsets was fixed at 100 ms; randomly, one in four stimulus events was a "null" event in which no stimulus was presented. The overlap between successive trials was removed by subtracting the averaged null event from the other stimulus conditions. Pilot experiments demonstrated that the null-subtracted responses were practically identical to responses measured with a longer stimulus onset asynchrony of 400 ms (data not shown) but with a higher signal-to-noise ratio given the increased number of trials. Because of the large number of stimulus conditions (16 locations plus 4 null events), the average presentation frequency for a given stimulus location was 0.5 Hz, slow enough to not cause attenuation [Chen et al., 2005]. In a single MEG/EEG session with 40–50 min of stimulus presentation (separated into 3-min blocks to allow subjects rest periods), ∼800–1,000 trials were acquired for each stimulus location.

### MRI and fMRI Image Collection

Subjects were scanned with a GE 3T scanner using a GE 8-channel phase array head coil. Two high-resolution T1 images were acquired to generate cortical surface models (TR = 10.5 ms, flip angle = 15°, bandwidth = 20.83 kHz, 256 × 192 matrix, 180 sagittal slices, 1 × 1 × 1 mm³ voxels). Proton density weighted images were acquired for reconstruction of the skull and scalp boundaries (flip angle = 5°). Echo-planar imaging was used to obtain T2*-weighted functional images every 2 s for 30 slices in the

axial plane with $3.125 \times 3.125 \times 3.5$ mm$^3$ voxels (TR = 2,000 ms, TE = 30 ms, flip angle = 90°, bandwidth = 62.5 kHz, $64 \times 64$ matrix, 200 mm FOV). For each functional imaging session, a coplanar T1-weighted structural scan was also acquired to align the lower resolution functional data with the cortical surface.

## Correction of Distortion in Structural and Functional MRI Images

Because structural and functional MRI data were used to constrain source modeling, it was critically important to correct for the significant image distortions caused by gradient nonlinearities and B0 magnetic field imhomogeneities. In-plane gradient warping was corrected online, and through-plane gradient warping was corrected offline by applying a predefined, scanner specific nonlinear transformation [Jovicich et al., 2006]. B0-inhomogeneity distortions in fMRI data were corrected using the reversing gradient method in which a pair of test images with opposite phase-encode polarity was acquired to estimate a displacement field [Chang and Fitzpatrick, 1992; Morgan et al., 2004; Reinsberg et al., 2005]. The resulting displacement field was then applied to full-length EPI fMRI images with identical slice prescriptions as the test images.

## Cortical Surface Modeling

T1-weighted MRI images were used to create a model of the cortical surface [Dale and Sereno, 1993; Dale et al., 1999; Fischl et al., 1999]. The cortical reconstruction algorithm is a multistep process that relies on differences in contrast between the different tissue types. Voxels corresponding to the skull and scalp were first stripped away. Subcortical structures were filled in and the left and right hemispheres were separated. The boundary between the gray and white matter was identified and both the gray-white interface and the outer cortical surface were modeled as continuous sheets. Careful manual editing of the white matter segmentation was performed to obtain accurate reconstructions of the cortical surface. After correcting for holes and smoothing, these surfaces can be "inflated" to unfold the cortex, or completely flattened after making cuts. fMRI data were sampled onto the cortical surface using a vector-search method in which the activation at a given cortical location was assigned to be that of the highest SNR voxel (most likely the one containing the largest fraction of gray matter) a short distance (up to 2 mm) along the vector normal to the surface [Hagler et al., 2006].

## Within-Subject Analysis of Event-Related or Block-Design fMRI Data

Random-order multi-block design fMRI data were analyzed using AFNI's 3dDeconvolve [Cox, 1996; Ward, 2000]. Image time series were first volume-registered to correct for motion artifacts using AFNI's 3dvolreg. The motion estimates from 3dvolreg were supplied to 3dDeconvolve as additional regressors to further reduce the contribution of motion to activation patterns, and a quadratic polynomial was used to fit the baseline. Fit coefficients and F-statistics were generated using general linear tests for the area under the curve of the hemodynamic response function, the amplitude of which was allowed to freely vary across a period of 10 s (at each of five post-stimulus TRs). General linear tests were also constructed for comparisons between task conditions. F-statistics were used to apply a statistical threshold to the fit coefficients, which were then displayed on the inflated cortical surface model described above.

## Phase-Encoded Retinotopic Mapping

Procedures for the acquisition and analysis of phase-encoded fMRI data have been described in detail previously [Hagler and Sereno, 2006; Hagler et al., 2007; Sereno et al., 1995]. Briefly, retinotopic maps of polar angle were measured using a wedge revolving around a central fixation point. Eccentricity was mapped using an expanding or contracting ring. Fourier transforms of the fMRI time series were computed to estimate the amplitude and phase of periodic signals at the stimulus frequency (eight cycles per 512-s scan), with phase corresponding to the preferred stimulus location for a given voxel. Subjects were scanned with equal numbers of scans with counterclockwise or clockwise stimulus revolutions. Similarly for eccentricity mapping, expansion and contraction scans were counterbalanced. Visual field sign was calculated from phase-encoded polar angle and eccentricity mapping data, allowing for the identification of the borders of visual areas [Sereno et al., 1994, 1995].

## MEG/EEG Forward Solution

Forward solutions were calculated using the boundary element method (BEM) [de Munck, 1992; Mosher et al., 1999; Oostendorp and van Oosterom, 1989]. High-resolution anatomical MRI data were used to identify and create surface tessellations for the following three layers: inner skull, outer skull, and outer scalp [Fuchs et al., 1998; Yvert et al., 1995; Zanow and Peters, 1995]. Proton-density weighted scans (rather than T1-weighted) were used for this purpose as these scans display good contrast between skull and CSF. Note that unlike EEG, MEG signals are less sensitive to the conductivity profile of the head–largely due to the low conductivity of the skull that confines almost all current within it–and thus only the inner skull boundary is truly required for the MEG forward solution; in this study however, all three surfaces were used for both EEG and MEG BEM forward solutions.

## Registration Between MRI and MEG/EEG Reference Frames

To determine the registration matrix defining the rigid body registration between MRI and MEG/EEG reference
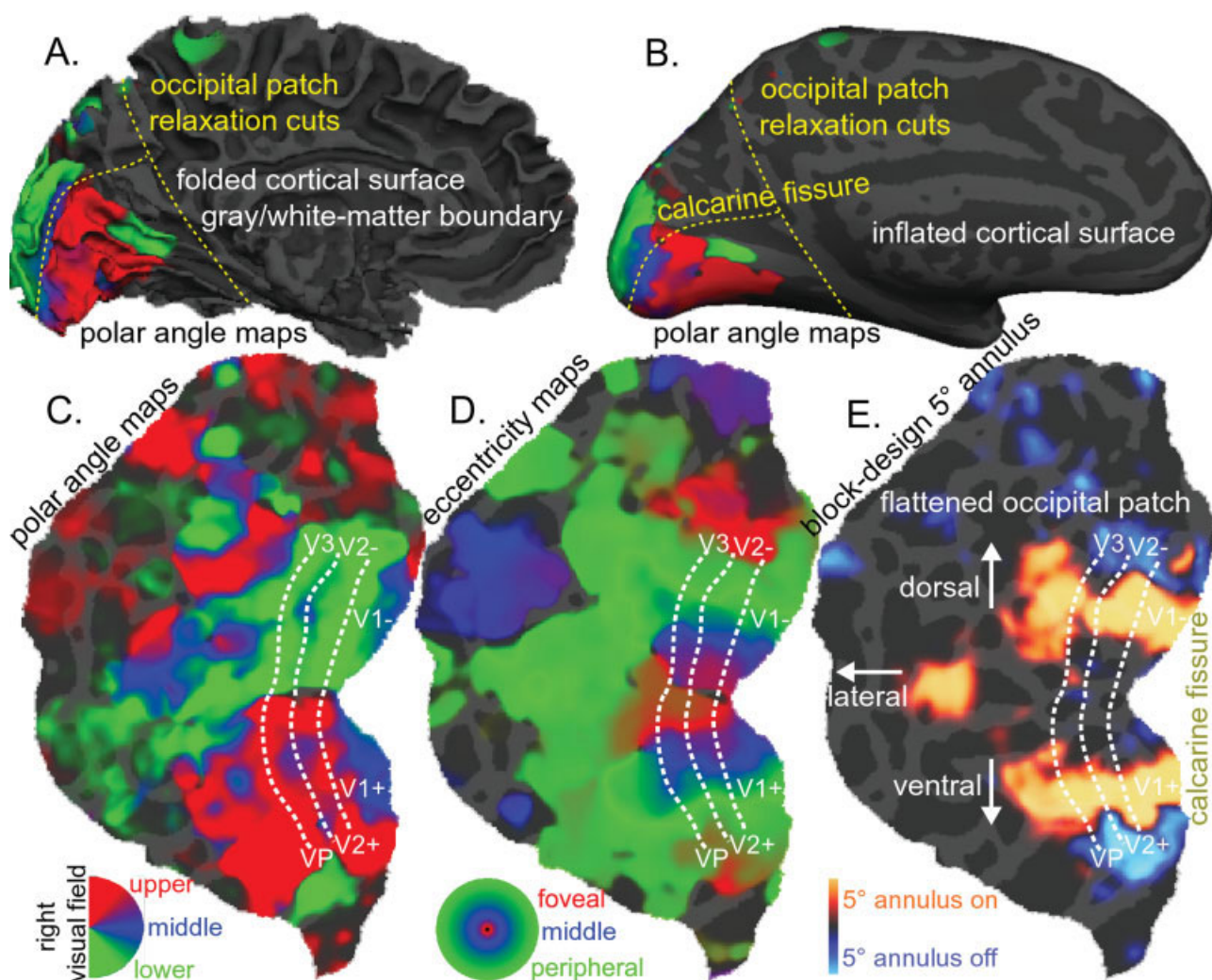
**Figure 1.**

Retinotopic maps acquired with 3T fMRI from Subject 1. (**A**) Polar angle maps superimposed on folded cortical surface (boundary between gray and white-matter) of left hemisphere. (**B**) Polar angle maps on inflated cortical surface. (**C**) Polar angle maps on flattened representation of the left hemisphere occipital cortical surface, with relaxation cuts along the calcarine fissure (shown in A and B as yellow dashed lines). Preferred (contralateral) polar angle is represented by colors indicated by legend. (**D**) Eccentricity maps. (**E**) Activation from flashing checkerboard annulus at a fixed eccentricity of 5° (±0.75°) visual angle. 18–22 s "on" blocks alternated with similar blocks of central fixation with no visual stimulation. [Color figure can be viewed in the online issue, which is available at www.interscience.wiley.com.]

frames, additional points on the scalp surface were recorded with the Polhemus FastTrack 3-D digitizer and then manually aligned to a surface representation of the outer scalp surface using a graphical interface written with MATLAB.

## Construction of a Retinotopic Model of the Generators of Evoked Visual Responses

Using information derived from structural MRI and phase-encoded fMRI retinotopic mapping, a model of the cortical sources of evoked visual responses was generated for each subject. Field sign reversals were used to manually identify the borders of early visual areas [Sereno et al., 1995]. Within each visual area, the preferred polar angle tends to change smoothly as a function of position along the cortical surface, forming retinotopic maps of visual space (see Fig. 1). For each subject, these maps were used to define the expected location of maximal activation in response to each of the 16 visual field locations used to elicit VEPs/VEFs. This was done separately for visual areas V1, V2, and V3. Dipoles were manually picked by making paths—with roughly equal spacing between individual surface vertices—along the appropriate iso-eccen-

tricity band (5° visual angle) in each visual area. The 5° visual angle iso-eccentricity band was identified on the basis of phase encoded eccentricity maps and confirmed with the block design annulus activation maps (Fig. 1D,E). Unlike the dSPM calculations, which typically use a subsampled cortical surface model, the dipole models informed by the retinotopy maps used vertices selected from the full-resolution cortical surface (∼0.8 mm intervertex distance).

Because the geometry of the cortical surface was measured for each subject, knowing the locations of peak activation also provided the expected orientation of the dipolar sources (i.e. perpendicular to the cortical surface). Thus, as the location of the visual stimulus changes, the cortical location and orientation of the modeled dipole for a particular visual area changes in a way determined by the MRI and fMRI data (Figs. 1 and 3). The estimated orientation of the cortical surface normal vector (perpendicular to the surface) can be somewhat variable, especially in highly curved patches of cortex. To model this diversity in the dipole orientations in single dipoles, the normal orientations were smoothed along the cortical surface with an 8-mm blurring kernel.

### Retinotopy-Constrained Source Estimation

The retinotopy-constrained forward solution is described by the following equation:

$$\mathbf{y}(t) = \mathbf{F}\mathbf{s}(t) + \mathbf{n}(t) \tag{1}$$

where $\mathbf{y}$, for each time point $t$, is a vector of measurements at each of 366 sensors (306 MEG, 60 EEG) at each of 16 iso-eccentricity stimulus locations—eight in right hemifield and eight in left hemifield—with a total of 5,856 measurements. $\mathbf{F}$ is a matrix of forward solution sensor amplitudes for each of several visual areas (sources). The size of $\mathbf{F}$ is the number of measurements times the number of sources. $\mathbf{s}$ is a vector of amplitudes for each source. $\mathbf{n}$ is a sensor noise vector. $\mathbf{y}$, $\mathbf{s}$, and $\mathbf{n}$, are each functions of time $t$, although $\mathbf{F}$ is time invariant. To fill the forward matrix with values, the forward solution for a particular dipole (i.e. a visual dipole cluster for one stimulus location) was obtained from a BEM gain matrix calculated for each vertex included in the model, generating amplitudes for each sensor. This was repeated for each stimulus location and each visual area, changing the dipole's cortical locations for each of the 16 stimulus locations. For the forward solution with free orientations and independence between stimulus locations, the number of "sources"—with 3 visual areas, 16 stimulus locations, and 3 vector components—was 144. With orientations fixed to the vector perpendicular to the cortical surface, the number of sources was 48. An alternative model configuration assumes that a given source has the same evoked response regardless of stimulus location. In this case, the data from multiple stimulus locations simultaneously constrain a single source waveform for each visual area modeled. With this "equality

constraint," the number of sources reduced to the number of visual areas. Given that the number of measurements is much larger (5,856) than the number of sources (3, 48, or 144 depending on constraints), the retinotopy-constrained inverse is highly overdetermined, unlike the underdetermined solutions provided by the cortically constrained minimum norm [Dale et al., 2000].

The following equation was used to define the inverse operator used to estimate source amplitudes at each time point

$$\mathbf{W} = (\mathbf{F}^{\mathbf{T}}(\lambda^2\mathbf{C})^{-1}\mathbf{F} + \mathbf{R}^{-1})^{-1}\mathbf{F}^{\mathbf{T}}(\lambda^2\mathbf{C})^{-1} \tag{2}$$

where $\mathbf{F}^{\mathbf{T}}$ is the transpose of the forward matrix $\mathbf{F}$, $\mathbf{C}$ is the noise covariance matrix (square in number of measurements), $\mathbf{R}$ is the source covariance matrix (square in the number of sources), and $\lambda^2$ is a regularization parameter equal to the mean of the diagonal elements of $\mathbf{FRF}^{\mathbf{T}}$ divided by the mean of the diagonal elements of $\mathbf{C}$, divided by the square of the assumed SNR (1 RMS). The assumed SNR value was roughly estimated from the sensor waveforms as the ratio between the evoked response and the baseline deflections. The inverse operator $\mathbf{W}$, was applied to the measured data as follows:

$$\hat{\mathbf{s}}(t) = \mathbf{W}\mathbf{y}(t) \tag{3}$$

where $\hat{\mathbf{s}}$ is the estimated source vector and $\mathbf{y}$ is the measurement vector, each functions of time $t$. The size of $\mathbf{W}$ is the number of sources times the number of measurements. The residual error was calculated as:

$$\mathbf{e}(t) = \mathbf{F}\hat{\mathbf{s}}(t) - \mathbf{y}(t) \tag{4}$$

Normalized residual error was calculated as the ratio between the variance of the residual error and the total variance of the data. The normalized residual errors for each sensor type—EEG, gradiometers, and magnetometers—were calculated separately and then averaged to get a measure of the residual error that was not affected by differences in units or number of sensors between the different modalities.

$\mathbf{C}$ was a diagonal matrix with variance values for each sensor calculated from the average baseline periods, averaged across all stimulus locations. Data from the different sensor types were scaled by predetermined values ($10^{13}$, $10^{15}$, and $10^6$ for gradiometers, magnetometers, and EEG electrodes respectively) to remove the orders of magnitude differences in scale between them, in order to ensure numerical stability. For independent stimulus locations, $\mathbf{R}$ was equal to the identity matrix (1's for diagonal values, 0's elsewhere). For the smoothness constraint, off-diagonal elements of $\mathbf{R}$—corresponding to the covariance between different stimulus locations within one visual area—were assigned non-zero values; the closer these values were to 1, the tighter the smoothness constraint. These off-diagonal values were set to 0.999 for nearest neighbor stimulus locations (within a visual area) and decreased with increasing distance according to the following equation:

$$r(k) = f^k \qquad (5)$$

where $r$ is the value assigned to the off-diagonal elements of **R**, $f$ is the smoothness constraint factor (equal to 0.999), and $k$ is the number of neighbor steps between two stimulus locations. For the equality constraint, within visual area off-diagonal elements could all be set to 1, but the equivalent action taken was to simply model one source per visual area and construct **F** such that the gain vectors for each stimulus location were arranged into a single column for a given visual area.

### Additional Nonretinotopic Dipoles

In some analyses (see Results and Supp. 4), additional dipoles were included in the forward solution to model cortical areas other than V1, V2, and V3 that may contribute to the evoked response. These additional dipoles were modeled as nonretinotopic, such that their responses did not vary as a function of stimulus location. Dipole orientations were allowed to freely rotate over time by modeling three orthogonal components, but the orientations and amplitudes for these dipoles were constrained by the data from all stimulus locations.

### EEG Conductivity Calibration

As mentioned above, conductivity values for brain, skull, and scalp are required for accurate modeling of EEG sources. If EEG data is analyzed alone, only relative conductivity values for the three different tissues is required (e.g. 1:0.04:1); but inaccurate conductivity values for the EEG forward solution will result in a mismatch in the amplitude of modeled source strengths for integrated EEG and MEG data, degrading the accuracy of localization. Realistic skull conductivity values can be chosen from published values [Hoekema et al., 2003], but conductivity values may vary between subjects, and inaccurate conductivity values could affect source localization accuracy. We used an iterative search method to find the scaling factor applied to the EEG forward solution that resulted in the lowest total residual error—across all sensors and stimulus locations, within a time range of 80–100 ms post-stimulus—for the retinotopy-constrained inverse with equality constraint. The assumed conductivity values were 0.3, 0.012, and 0.3 S/m for brain, skull, and scalp, respectively. With those preconditions, the best fitting scaling factors for subjects 1 and 2 were 0.98 and 0.85, respectively. The minima were relatively broad; for example, for subject 2, the fractional change in residual error between scaling factors of 0.85 and 1.0 was ~0.001. For the source estimates shown in Results, a scaling factor of 1 was used for both subjects.

### Dynamic Statistical Parametric Mapping (dSPM) for MEG and EEG

For purposes of comparison with retinotopy constrained source estimates, distributed source estimates were also calculated using the dSPM method [Dale et al., 2000]. The cortically constrained, fMRI biased, noise-normalized, $L_2$ minimum-norm, linear inverse was calculated for ~5,000 cortical surface dipoles (vertices) distributed across the cortical surface with an intervertex spacing of ~7 mm. For the fMRI bias, activation elicited by a block-design flashing checkerboard ring was used to set *a priori* weighting factors [Dale and Sereno, 1993; Dale et al., 2000; Liu et al. 1998]. In the source covariance matrix, off-diagonal terms were set to 0, diagonal terms corresponding to suprathreshold vertices (subjectively chosen, arbitrary threshold was applied to block-design annulus data shown in Fig. 1) were assigned a weighting of 0.9, and diagonal terms for subthreshold vertices were assigned a weighting of 0.1. The orientations of dipoles were allowed to vary freely by simultaneously fitting for each of three vector components. The noise covariance matrix was a diagonal matrix with variance values for each sensor calculated from the average baseline periods, averaged across all stimulus locations. dSPM source estimates were noise normalized as described previously [Dale et al., 2000]. The regularization parameter was calculated as described above for the retinotopy constrained inverse, with the same assumed SNR value of 1.

## RESULTS

### Visual Responses Measured With fMRI, MEG, and EEG

We used phase-encoded fMRI to measure the polar angle and eccentricity maps that span the convoluted occipital cortical surface (see Fig. 1). The borders between V1, V2, and V3/VP were identified based on field sign reversals [Sereno et al., 1995]. A block-design stimulus was also used to localize the cortex activated by a flashing checkerboard ring at an eccentricity of 5° visual angle (Fig. 1E). These fMRI data were used to construct retinotopic dipole models of the generators of the VER (see Methods).

Figure 2 shows the VERs measured with MEG and EEG for the subject whose fMRI data are shown in Figure 1, along with the corresponding stimulus locations. VEPs and VEFs exhibited large variations as a function of stimulus location, the pattern of which changed over time. In addition, response polarities varied substantially within a visual quarterfield. At 80-ms post-stimulus, a clear polarity reversal was observed for VEPs measured in upper and lower visual field locations (e.g. compare green EEG traces in Fig. 2A,B to those in Fig. 2C,D).

Average VEPs and VEFs between 80- and 90-ms post-stimulus are shown as contour plots in Figure 3. Ball and stick representations show the dipole orientations derived from MRI and fMRI data for V1, V2, and V3. Overall, the observed field and potential patterns match well with the patterns predicted by the MRI-derived dipoles for V1 (Compare Figs. 3 and 4). Contributions from V2 and V3 (Supp. Figs. 1 and 2), as well as other visual areas, are likely explanations for why the observed patterns are somewhat
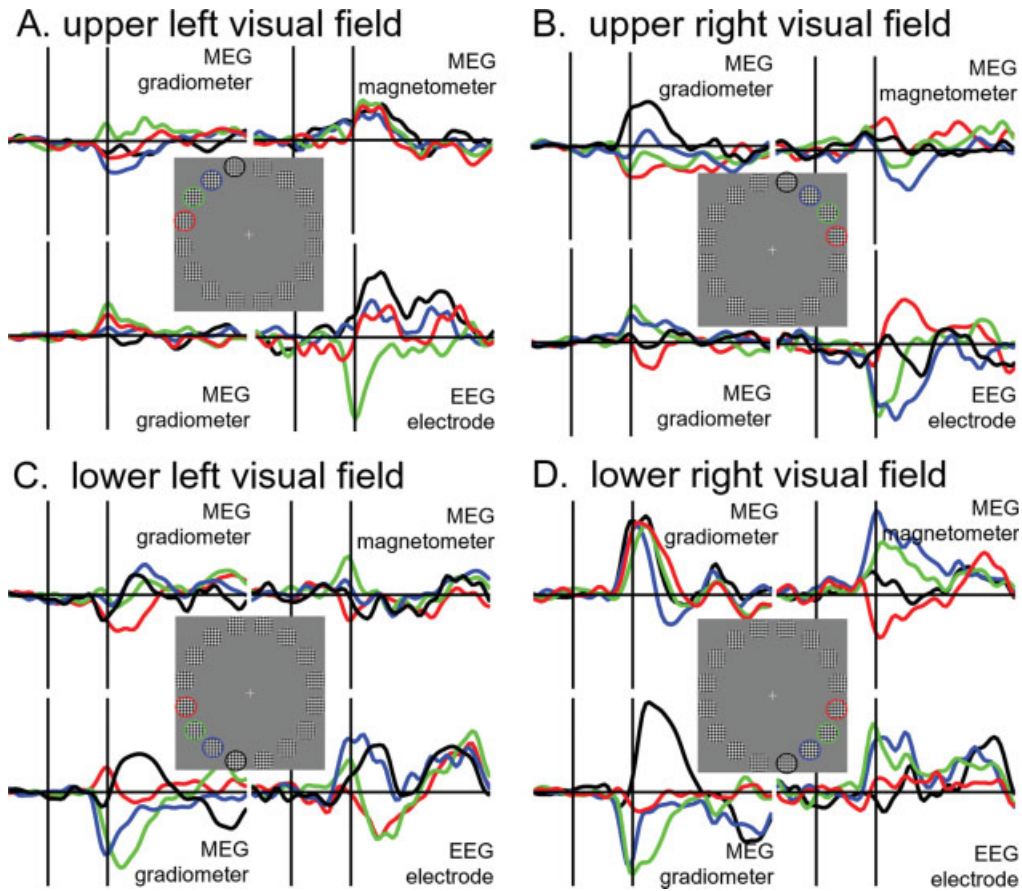
**Figure 2.**

MEG/EEG evoked responses to visual stimulation from Subject 1. Signals from two gradiometers, one magnetometer, and an EEG electrode at a mid-line occipital location. Vertical lines indicate time of stimulus onset and 80-ms post-stimulus. Vertical scales are ±60 fT/cm for gradiometers, ± 120 fT for magnetometers, and ±5 μV for EEG electrode (up = positive). Gray squares with colored circles indicate which colored trace corresponds to each stimulus location (n.b., no colored circles were present in the stimuli as presented to the subjects). [Color figure can be viewed in the online issue, which is available at www.interscience.wiley.com.]
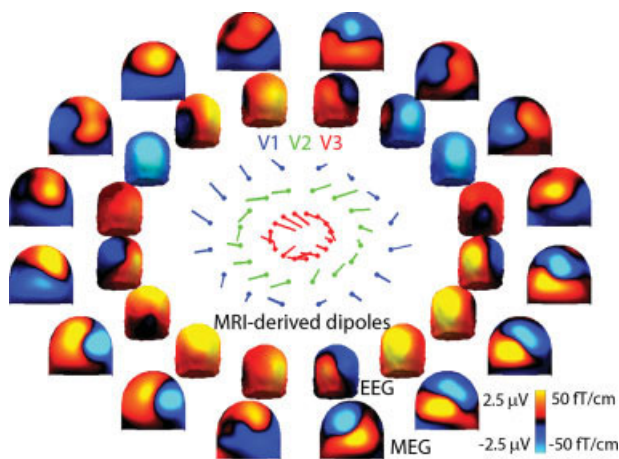


**Figure 3.**

MEG and EEG contour plots arranged at polar angles corresponding to 16 iso-eccentricity stimulus locations. MEG data (average amplitudes over 80- to 90-ms post-stimulus, gradiometers only) are interpolated onto the helmet surface (outer ring of contour plots) with red representing flux out of the head and blue representing flux into the head. EEG data is interpolated onto the outer scalp surface, with red representing positive scalp potentials and blue representing negative scalp potentials. Dipoles for V1, V2, and V3 (derived from structural and functional MRI data) are represented as ball and stick diagrams with the direction and length of the line indicating the dipole orientation components in the coronal plane. Data are from Subject 1. [Color figure can be viewed in the online issue, which is available at www.interscience.wiley.com.]
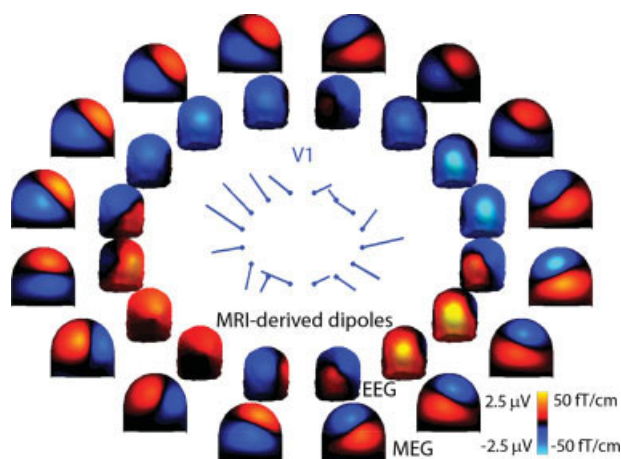
**Figure 4.**
Predicted MEG and EEG contour plots for V1. Predicted MEG and EEG data were generated for current dipoles derived from structural and functional MRI (see Methods). Plotting conventions are same as in Figure 3. [Color figure can be viewed in the online issue, which is available at www.interscience.wiley.com.]

more complicated than the simple dipolar patterns predicted by V1 alone. Large mismatches between the observed and predicted V1 patterns for particular stimulus locations (e.g. above right horizontal meridian) could also reflect errors in the dipole orientations predicted by MRI.

## Source Estimates Obtained With dSPM

As a basis for later comparison, a cortically constrained, fMRI biased, $L_2$ minimum-norm inverse solution (i.e. dSPM) was used to estimate source time courses from both MEG and EEG sensor data (see Methods). In Figure 5A, cortical surface maps of source statistics are shown for stimuli in each of the four quadrants of the visual field at 72-ms post-stimulus. Note the crossover of apparent activation between hemispheres due to the proximity of the modeled dipoles in the medial aspect of the two hemispheres. In addition, lower field stimuli are expected to activate V1 superior to the fundus of the calcarine sulcus as well as V2d and V3. Upper field stimuli activate inferior V1 as well as V2v and VP. The dSPMs shown, however, do not fit that expected pattern, instead displaying a more generalized spread of activation across visual cortex.

Regions of interest (ROIs) were created for visual areas V1, V2d, V2v, V3, and VP and used to extract average time courses for each. These time courses are shown in Figure 5B, and illustrate the high degree of crosstalk between neighboring visual areas when this inverse method is used. They each have essentially the same time course with varying amplitudes, something that is unrealistic given our understanding of the flow of activation through visual cortical areas. That the cortically constrained minimum-norm provides an inadequate solution

in this case is entirely expected from and consistent with a previous simulation study in which this method was estimated to have an effective resolution of ~20 mm [Liu et al., 2002]. That each of the visual areas is assigned practically the same source waveform reflects the ambiguity between the multiple sources resulting from their proximity and the minimal constraints imposed on the solution. In order to impose additional constraints however, additional *a priori* information is required.

## Retinotopy-Constrained Source Estimates

By allowing for dipoles at as many as 5,000 cortical locations, the cortically constrained minimum-norm is fundamentally underdetermined or ill-posed. Retinotopic mapping with fMRI provides the opportunity to drastically reduce the number of unknowns by fixing the dipole locations to those cortical locations that correspond to a given stimulus location in individual visual areas. As described in Methods, dipole locations were chosen for each stimulus location for V1, V2, and V3. Dipole orientations were fixed to be perpendicular to the cortical surface at each location. The estimated source waveforms displayed large variations between stimulus locations (Fig. 6A).

With the retinotopy-constrained inverse just described, source waveforms were estimated independently for each stimulus location. It is reasonable to assume, however, that the source amplitudes smoothly vary as a function of stimulus location. That is, neighboring stimulus locations should evoke similar source waveforms at neighboring cortical locations within a given visual area. This smoothness constraint was implemented by setting the appropriate off-diagonal terms of the source covariance matrix to non-zero values (see Methods). As required by this model, the individual source waveforms for each stimulus location—for a given visual area—were more similar to each other and exhibited a smooth transition between neighboring locations (Fig. 6B).

As the off-diagonal covariance terms are increased, the smoothness constraint becomes stronger. With values of 1, the smoothness constraint becomes an equality constraint. Source estimates for all stimulus locations are forced to be identical across a given visual area, or equivalently, a single source waveform is estimated for each visual area modeled. Thus instead of attempting to assign responses to individual dipoles, responses to all stimulus locations are fitted to a collection of dipoles. The dipoles were modeled to move across the cortical surface in a path predicted by the fMRI retinotopic maps, changing orientation to match the curvature of the cortical surface modeled from structural MRI. These dipole paths constitute a signature for each visual area (Fig. 4, Supp. Figs. 1 and 2) that allow for the unambiguous assignment of activity to each visual area over time, resulting in waveforms for each visual area that show clear differences in response latency (see Fig. 7).

Subject 1's V1 waveform estimate appears to exhibit a small, positive deflection peaking at 51 ms. A large nega-

## A. fMRI and cortically constrained dSPM



## B. ROI averages of dSPM source time courses
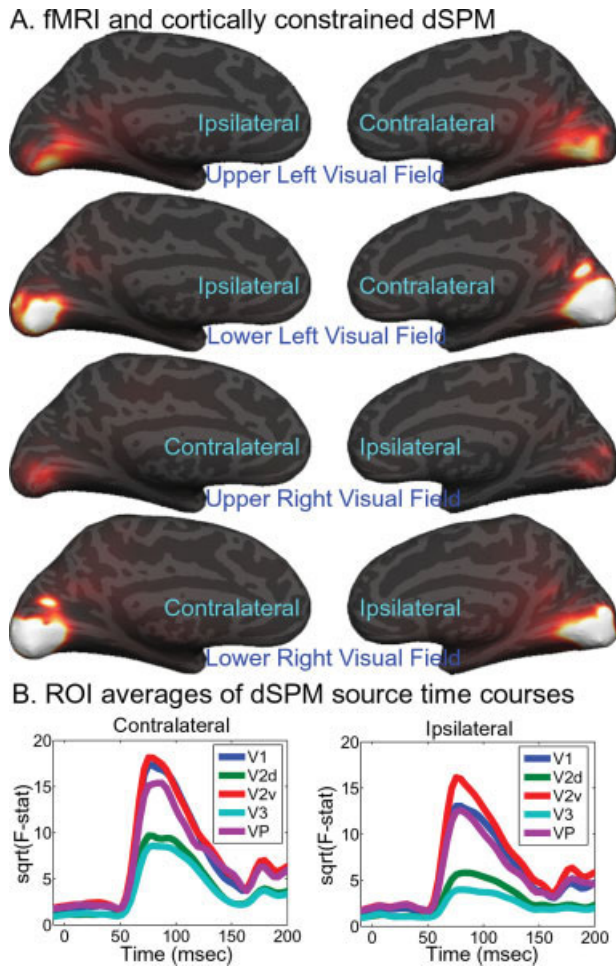


**Figure 5.**

Cortically constrained, fMRI-biased, noise-normalized, $L_2$ minimum-norm source estimates of visual evoked responses. (**A**) Medial, inflated views of cortical surface overlaid with dSPM statistics (see Methods) for visual responses evoked by stimuli in upper and lower, right and left quarterfields (eccentricity = $5°$, polar angles = $56°$ $124°$, $236°$, $304°$). (**B**) ROI average time courses for V1, V2, and V3 derived from dSPM. Source estimate statistics were averaged within hand-drawn cortical surface-based regions of interest (based on fMRI retinotopy maps and calculated field sign; see Methods), and then collapsed across hemispheres and stimulus locations into averages for contralateral or ipsilateral stimuli. [Color figure can be viewed in the online issue, which is available at www.interscience.wiley.com.]

tive peak follows immediately at 78 ms (Fig. 7A). The polarity of the deflections are related to the laminar distribution of cortical current sinks and sources [Creutzfeldt et al., 1966; Einevoll et al., 2007]; this will be discussed further below. V2 exhibits a similar pair of positive and negative peaks at 63 and 91 ms. V3 exhibits a larger positive peak at 68 ms, also followed by a negative peak at 112 ms. Subject 2 displays a similar pattern of activation across V1,

V2, and V3, although with slightly different latencies (Fig. 7B). Future work with a large cohort of subjects will provide a better sample of the inter-subject variability, but this comparison is a preliminary demonstration that the retinotopy-constrained inverse method yields source estimates that are roughly consistent across subjects. Another demonstration of the robustness of the method is that source estimates derived from MEG-only were generally similar to those derived from EEG-only, although the EEG-derived estimates appear considerably noisier (Fig. 7C,D).

The initial positive deflection of V3 seems to be in opposition to the negative deflection of V1, perhaps suggestive of crosstalk between the two source estimates. Crosstalk between two sources $i$ and $j$ can be directly calculated [Liu et al., 1998] as:

$$c_{ij}^2 = \frac{\left|(\mathbf{WF})_{ij}\right|^2}{\left|(\mathbf{WF})_{ii}\right|^2} \qquad (6)$$

with $W$ being the inverse operator and $F$ the forward matrix. Crosstalk between the three visual areas was calculated with a variety of constraints (Table I). Crosstalk was highest for forward models with independent sources for each stimulus location and free orientations. Crosstalk for fixed orientation sources was much lower; when the equality constraint was used, even lower. The result is that crosstalk between the V1 and V3 dipole models cannot explain the large positive deflection seen in the V3 source estimates (see Supp. Fig. 3).

## Analysis of Residual Error

To prevent over-fitting the data—i.e. where noise dominates the source estimates—all of the source estimates were made with regularized inverse solutions using an assumed SNR of 1 RMS. This means that the fitted sensor waveforms are not necessarily identical to the actual data, even when the problem is under-determined. The difference between the fitted sensor waveforms and the actual data is the residual error, and in fact none of the methods presented here achieve zero residual error (see Fig. 8). The dSPM method yields the lowest residual error, as low as 10% during the largest visual evoked response, and as high as 30–40% during the baseline. That this method fits the baseline noise as well as it does reflect its underdetermined nature due to the large number of free parameters (∼15,000 per time point). Greatly reducing the number of dipoles and fixing their locations increases the residual error during the peak evoked response, as does fixing their orientations, and greatly increases the residual error during the baseline period (Fig. 8A).

Adding the smoothness or equality constraints—i.e., assuming that neighboring stimulus locations give rise to similar or identical source waveforms—increases the residual error further (Fig. 8B), yet results in more plausible
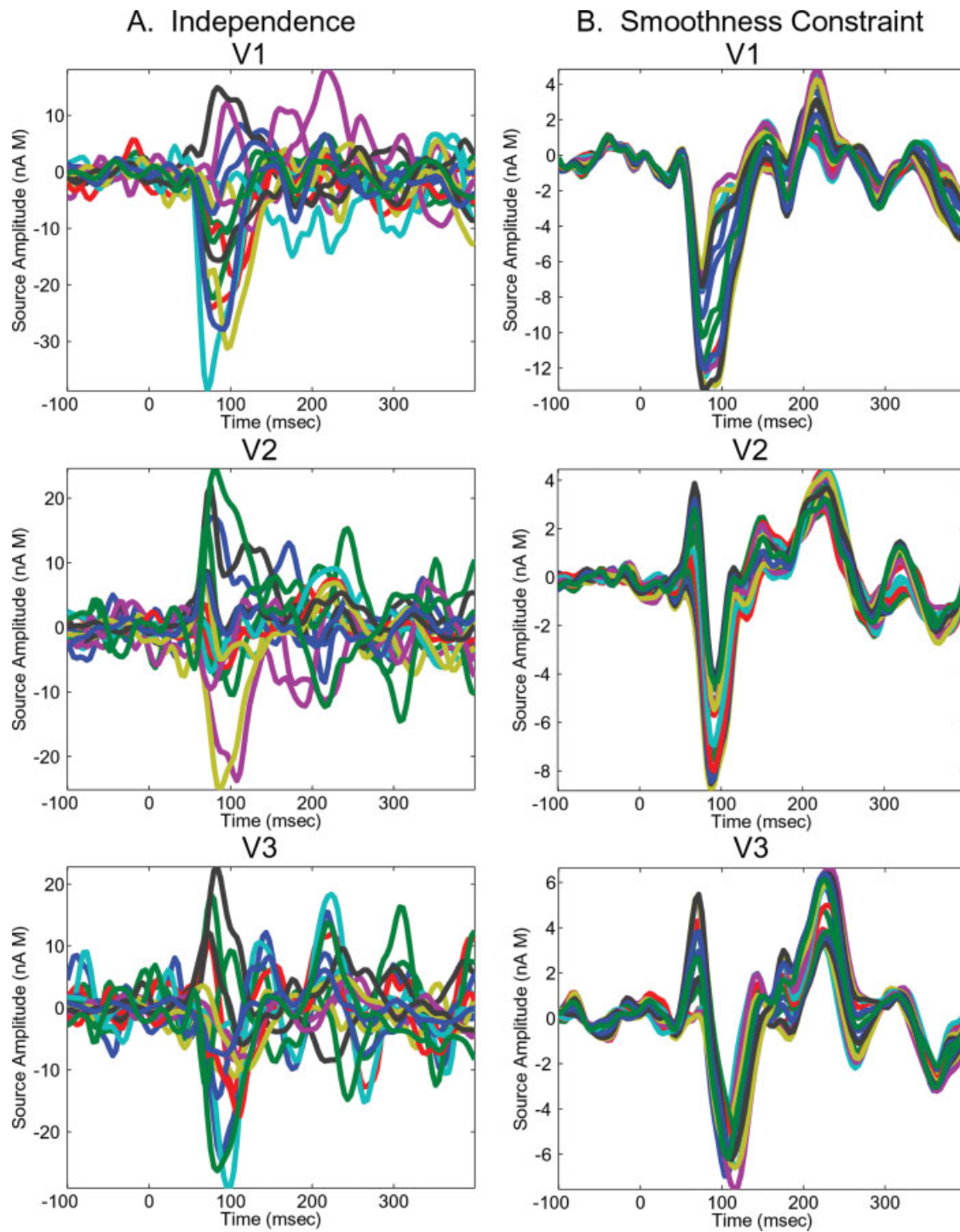
**Figure 6.**

Retinotopy-constrained source estimates with independence between stimulus locations or smoothness constraint. Dipole locations were chosen for each stimulus location for V1, V2, and V3, and orientations were fixed to be perpendicular to the cortical surface at each location. (**A**) Sources waveforms for each stimulus location were estimated independently. (**B**) Source waveforms were assumed to smoothly vary with stimulus location (see Methods). [Color figure can be viewed in the online issue, which is available at www.interscience.wiley.com.]

**TABLE I. Crosstalk between visual areas with varying constraints**

| Constraint | | CT(V1,V2) | CT(V1,V3) | CT(V2,V3) |
|---|---|---|---|---|
| Independent, | min | 0.046 | 0.004 | 0.041 |
| free orientations | max | 1.904 | 0.304 | 0.553 |
| Independent, | min | $2.1 \times 10^{-5}$ | $9.7 \times 10^{-6}$ | $1.2 \times 10^{-6}$ |
| fixed orientations | max | 0.687 | 0.082 | 0.374 |
| Equality, fixed orientations | | $3.2 \times 10^{-8}$ | $1.9 \times 10^{-7}$ | $3.8 \times 10^{-9}$ |

estimated source waveforms in the sense that similarity across stimulus locations is enforced. Furthermore, the residual error during the baseline period is extremely high. Baseline noise, which presumably varies randomly with respect to stimulus location, is inconsistent with a model that predicts systematic changes in dipole orientation and location as a function of stimulus location. The fact though, that the equality constraint provides a relatively poor fit to the data (~58% residual error between 70 and 90 ms post-stimulus) suggests that there may be errors or oversimplifications in the retinotopic dipole model.

There are a variety of potential sources of error in the dipole model. We will describe several—and possible ways to deal with them—in the Discussion. Here we will consider what may be the most likely source of error; that is, random errors in the specification of the dipole orientations. Assuming that the carefully edited cortical surface reconstruction is largely accurate, the modeled dipole orientations rely upon accurately placed dipole locations based on the sometimes noisy fMRI retinotopic maps. Accordingly, if the location chosen is 1 or 2 mm away (i.e. 1 or 2 vertices) from the true center of activation, this may affect the estimated dipole orientation and hence the source estimates and residual error from the retinotopy-constrained inverse method.

We investigated this issue by calculating the differences in dipole orientations between vertices included in the retinotopy-constrained dipole models and their neighboring vertices. The average differences for 1, 2, 3, 4, and 5 vertices away were 18°, 30°, 37°, 41°, and 44°, respectively. To simulate the effect of this type of error, simulated sensor data was generated by applying the forward solution to the source waveforms estimated from actual data using the equality constraint. Gaussian noise with the same standard deviation as the baseline period of the actual data was added to the simulated sensor data. Source waveforms were then estimated from the simulated data using alternate forward models containing random errors in each dipole's orientations, averaging 0°, 18°, 30°, 37°, 41°, or 44°. As the size of the dipole orientation errors was increased, the residual error of the simulated source estimates also increased (Fig. 9A). Interestingly, shape and timing of the simulated source estimates were relatively insensitive to the orientation errors (Fig. 9B,C). Repeating these simulations with independent estimates for each stimulus location, we found that the simulated source esti-

mates were highly sensitive to random orientation errors (see Fig. 10). Thus, using full dipole paths, rather than single dipoles, makes the source estimates less sensitive to potential errors induced by non-systematic mislocalization of a few dipoles.

## Additional Sources

It is an understatement to say that V1, V2, and V3 alone are not responsible for generating the early visual evoked response. MT, for example, is known to be activated as early or earlier than V1 [Raiguel et al., 1989; Schmolesky et al., 1998]. Retinotopic mapping of MT is possible [Huk et al., 2002], but its much larger receptive fields may mean that the optimal dipole locations for the different stimulus locations would be in a relatively tight cluster near the center of MT. In addition, the presence of multiple maps in a small area makes the selection of dipole locations more arbitrary and error prone. To simplify, MT was represented as a nonretinotopic dipole, with a fixed response across stimulus locations. Each hemisphere was given its own, independent source for MT, at a location chosen from fMRI retinotopic maps. Because of uncertainty in the precise location and orientation of dipoles in MT, the orientation was allowed to freely vary across time. The source time courses estimated for MT have peak latencies and amplitudes roughly similar to V1, V2, and V3, but the source estimates for V1–V3 are minimally changed with the addition of these additional sources (Supp. Fig. 4). The residual error decreased slightly with the addition of the MT dipoles across the duration of the evoked response (Supp. Fig. 4E).

Simulations may prove useful for testing whether the source estimates from the retinotopy-constrained inverse are sensitive to additional, unmodeled sources. The source waveforms estimated for the normal component of the MT dipoles, along with the source estimates for V1–V3, were used to simulate sensor waveforms. We then used the retinotopy-constrained inverse to estimate source waveforms from the simulated data. The simulated source estimates for V1–V3 were rather insensitive to the additional sources, regardless of whether MT dipoles were included in the inverse (Supp. Fig. 5).

## DISCUSSION

We have developed a method for estimating visual evoked MEG and EEG responses in individual visual areas that attempts to resolve the inherent ambiguity between closely spaced dipolar sources. This method uses structural and functional MRI to determine dipole locations and orientations and uses data from multiple stimulus locations to simultaneously constrain the solutions. Source waveforms are assumed to be identical, or smoothly varying, across stimulus locations, within a given visual area. The use of multiple stimulus locations is critical to deriving
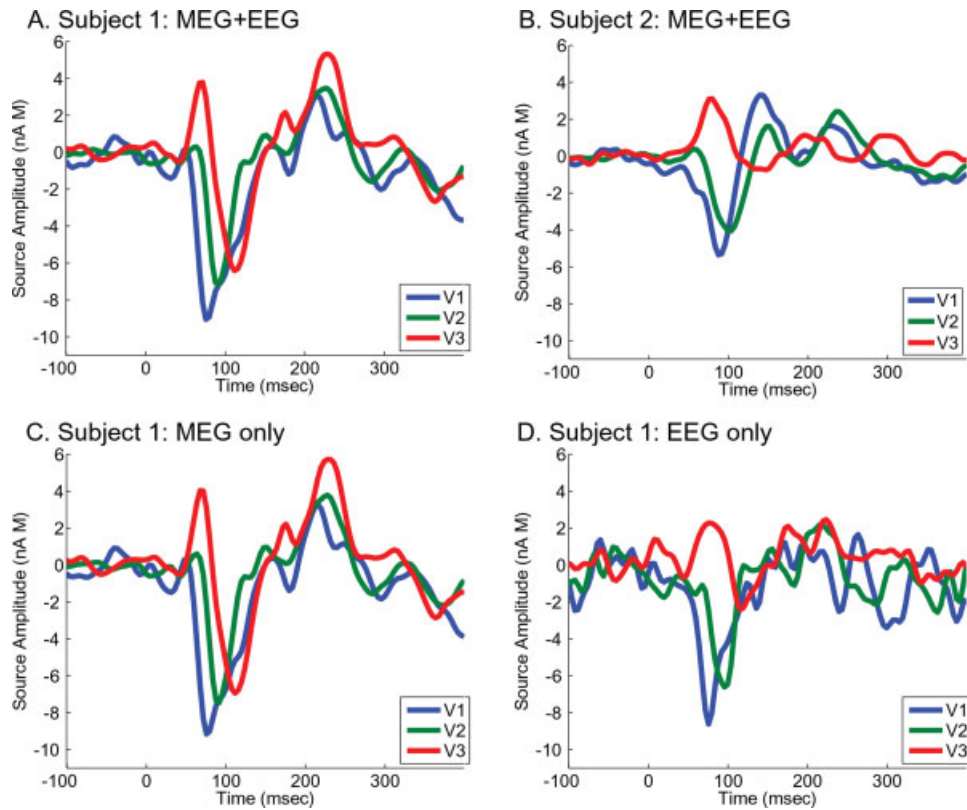
**Figure 7.**

Retinotopy-constrained source estimates assuming equality of source amplitudes across 16 stimu-
lus locations. (**A**) Source estimates for Subject 1 generated for each visual area, constrained by
the MEG and EEG data from the multiple stimulus locations. (**B**) Source estimates generated
from Subject 2's MEG and EEG data (with dipoles modeled from Subject 2's MRI data). (**C**)
Source estimates for Subject 1 using only MEG data. (**D**) Using only EEG data. [Color figure can
be viewed in the online issue, which is available at www.interscience.wiley.com.]
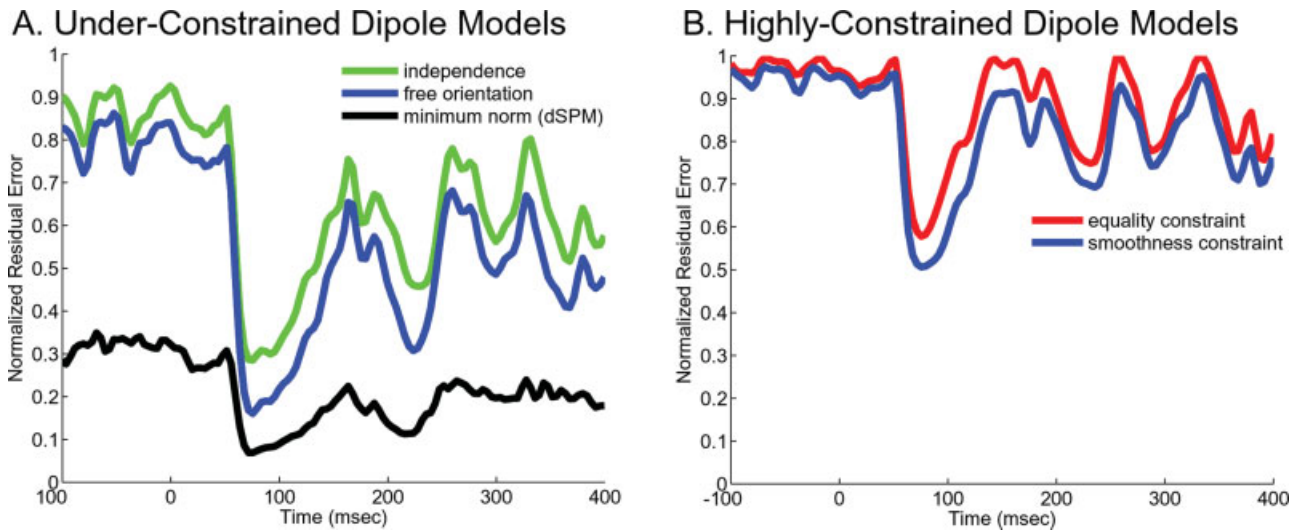


**Figure 8.**

Residual error of visual evoked source estimates. (**A**) Normalized
residual error for undercontrained but regularized (assumed SNR
= 1 RMS) source models including (1) retinotopy-constrained
dipole locations and orientations, (2) retinotopy-constrained
dipole locations with free orientations, and (3) $L_2$ minimum norm
(dSPM). All three models allow independence between stimulus

locations. (**B**) Normalized residual error for retinotopy-con-
strained source estimates with (1) smoothness constraint, and (2)
equality constraint. Normalized residual error was calculated as
the ratio between the variance of the residual error and the total
variance of the data. [Color figure can be viewed in the online
issue, which is available at www.interscience.wiley.com.]

source waveforms that are relatively insensitive to random errors in the specification of the dipole model.

Some early attempts to model the VEP focused primarily on V1 and demonstrated that fitted dipole orientations or locations varied as a function of stimulus location in a way consistent with the idealized retinotopic topography of V1 [Aine et al., 1996; Clark et al., 1995; Jeffreys, 1968; Slotnick et al., 1999]. Slotnick et al. used multiple, iso-eccentricity stimulus locations to simultaneously constrain the source waveforms, but dipole locations were not constrained and V1 was the only area modeled. Additional studies modeled the VEP with a larger number of dipoles [Aine et al., 2000; Di Russo et al., 2001, 2003, 2005; Martinez et al., 1999, 2001; Vanni et al., 2004] and introduced fMRI data to fix dipole locations [Di Russo et al., 2005; Vanni et al., 2004] and orientations [Vanni et al., 2004]. One shortcoming of the models used in those studies is that single dipoles were made to model multiple visual areas; for example, V2, V3, and V3A modeled with a single dipole, or a single dipole for ventral occipital. In the absence of the simultaneous constraint across multiple stimulus locations, this type of simplification of the model was necessary due to problems with crosstalk and ambiguity between closely situated dipoles.

Other studies of VER sources used minimum-norm distributed source methods [Ahlfors et al., 1992; Sharon et al., 2007]. The noise-normalized minimum-norm (i.e. dSPM) source estimates for the earliest VER component were shown to agree well with fMRI activations, particularly when MEG and EEG were combined [Sharon et al., 2007]. Our results show that the dSPM method, even when MEG and EEG are combined, does not provide plausible time courses for the early visual areas; rather, the estimated time courses for the different visual areas are remarkably similar. This is probably due to the high level of crosstalk between neighboring dipoles and the relatively large point spread function (~20 mm or more) of the dSPM method [Liu et al., 2002].

The retinotopy-constrained inverse method described in the current study has integrated useful features of methods used in these previous studies including: (1) using single-subject fMRI and MRI data to fix the locations and orientations of modeled dipoles, (2) simultaneously fitting for multiple visual areas, (3) and constraining the solutions with multiple stimulus locations. A significant improvement comes from constraining the solutions for separate visual areas with a collection of stimulus locations. This provides a kind of signature for each visual area that is more distinct than simply a location and orientation. Crosstalk between areas is reduced, resulting in improved separation between source estimates for individual areas.

### Temporal Components of Source Waveforms

Previous studies of pattern-onset VEPs in humans have identified the C1 component, which occurs between 60 and 100 ms post-stimulus and reverses in polarity between upper and lower field stimuli [Butler et al., 1987; Clark et al., 1995; Di Russo et al., 2001, 2003; Jeffreys, 1968; Jeffreys and Axford, 1972; Jeffreys and Smith, 1979; Mangun, 1995; Martinez et al., 1999]. This timing matches that of the large negative peak we observe in the V1 source waveform and the polarity is consistent as well. Negative polarity represents a dipole pointing perpendicular to the cortical surface, toward the white matter. For an upper field stimulus, the idealized V1 dipole is located on the lower bank of the calcarine sulcus, so negative polarity results in a negative potential on the scalp surface. A lower field stimulus with the negative dipole located on the upper bank of the calcarine results in a positive scalp potential. The source waveforms for V2 and V3 exhibited similar negative peaks, delayed by 13 and 23 ms, respectively. This latency difference between V1 and V2 is consistent with that observed in awake, behaving monkeys [Schroeder et al., 1998].

Visual areas V2 and V3, and to a much lesser extent V1, also exhibited small positive deflections preceding the large negative peaks. This biphasic response is very similar to recordings made from the cortical surface of V1 in awake, behaving monkeys presented with patterned stimuli [Schroeder et al., 1991]. The shape of the cortical-surface VEP depends on the laminar pattern of cortical inputs [Creutzfeldt et al., 1966; Schroeder et al., 1991]. Initial thalamic input to layer 4 cells leads to depolarization of basal dendrites of layer 2/3 pyramidal neurons, resulting in a negative extracellular potential [Barth and Di, 1991; Einevoll et al., 2007]. Positive current traveling up the apical dendrites and returning to the extracellular space results in a positive extracellular potential in the upper layers. This forms a positive dipole that could explain the early positive deflections in the source waveforms. The large negative component is likely due to activation of the apical dendrites of pyramidal neurons [Barth and Di, 1991; Einevoll et al., 2007]. As positive current travels down to the somas and out into the extracellular space, this sets up a negative dipole. Later components in the source waveforms were likely a complicated combination of depolarization and hyperpolarization due to excitation and inhibition, as well as responses to the offset of the stimulus after 83 ms. The larger size of the early positive deflection for V3 compared to V1 and V2 may reflect differences in the timing of activation in particular cortical layers, but errors in the source estimates due to inaccuracies in the dipole models cannot be ruled out at this point.

### Factors Limiting the Accuracy of Source Estimates

Because the modeled dipole locations and orientations in the retinotopy-constrained model are exactly specified and not allowed to freely vary, the resulting source estimates are dependent on how accurately the dipole model is specified. That accuracy is limited by several factors, including simplifications made in constructing the retinotopic dipole models and technical considerations about the

## A. Residual Error for Increasing Random Dipole Errors
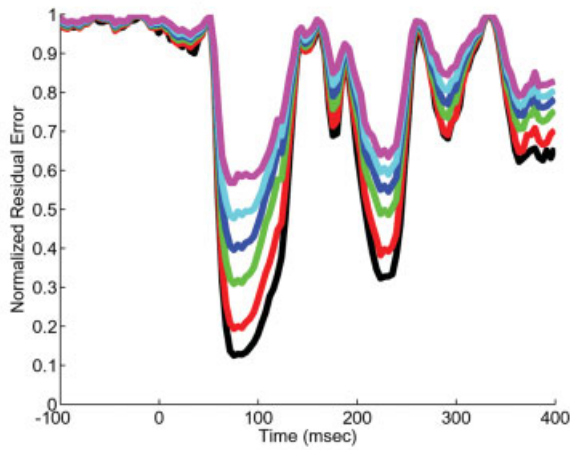
## B. Simulated Source Estimates with No Random Dipole Errors

## C. Simulated Source Estimates with 4 Vertex Random Dipole Errors

**Figure 9.**

## A. Residual Error for Increasing Random Dipole Errors
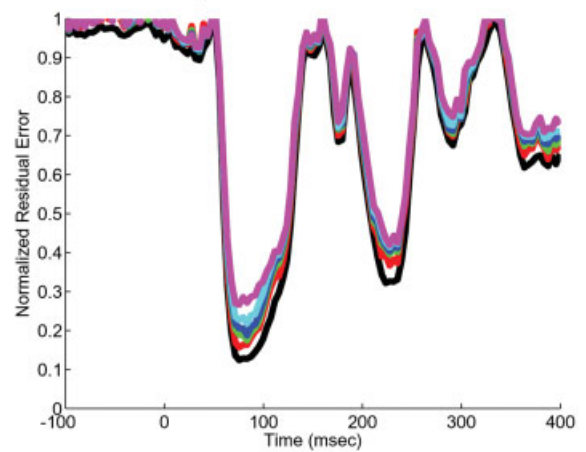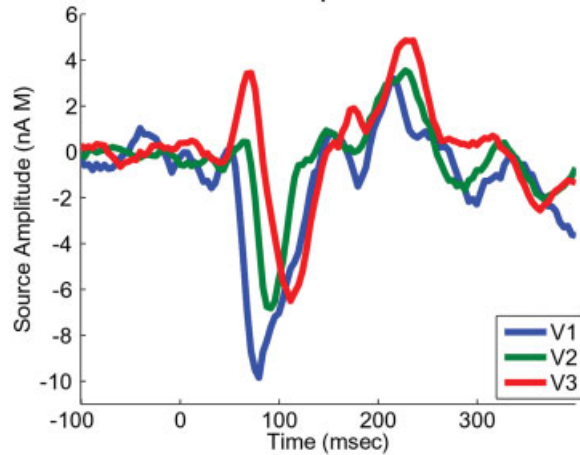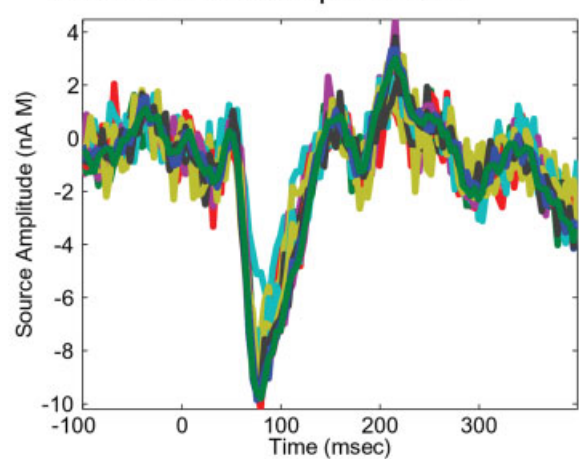
## B. Simulated V1 Source Estimates with No Random Dipole Errors
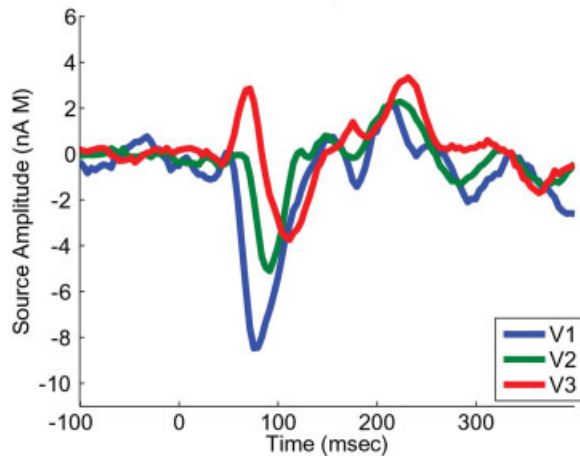
## C. Simulated Source Estimates with 4 Vertex Random Dipole Errors
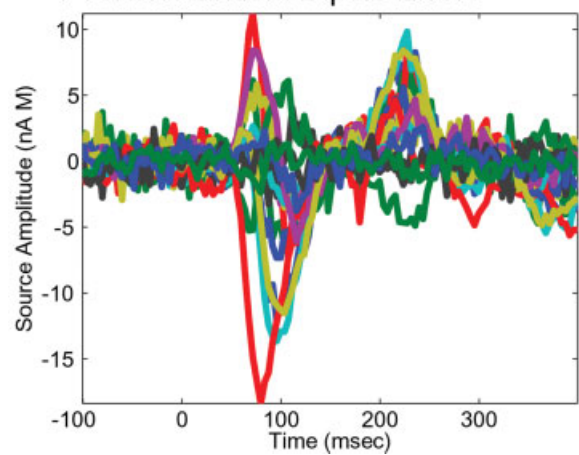
**Figure 10.**

imaging and analysis methods used. Simplifications we made included limiting the number of visual areas to three, ignoring potential differences between responses to upper and lower field stimulus locations, and assuming a single dipole for each stimulus location for a given visual area. Technical considerations include potential mismatches between fMRI and MEG/EEG data, registration between MRI, fMRI, and MEG/EEG data, accuracy of dipole locations and orientations specified by MRI/fMRI data, and accuracy of the forward model. Each of these factors could reduce the accuracy of the source estimates and therefore deserve careful consideration.

### Simplifications to Retinotopic Dipole Models

Given that there are more than 20 distinct areas in human visual cortex [Felleman and Van Essen, 1991], modeling only a few of these areas could result in significant residual error, even if those areas (i.e. V1, V2, and V3) are expected to produce the largest amplitude visual evoked responses. Because a collection of dipoles was used for each visual area, crosstalk between visual areas is very low; thus, even if a visual area is not included in the model, its activity should not be assigned to another visual area. This is important because it is likely that several visual areas that we have not modeled also contribute to the visual evoked response. Including additional retinotopic— or weakly retinotopic—areas may yield a better fit to the data, particularly at later time points, provided that accurate retinotopic maps can be obtained for those areas. Other, nonretinotopic areas that contribute to the evoked visual response can be modeled as dipoles with the same time course and orientation regardless of stimulus location.

One may question whether it is justifiable to assume that different stimulus locations will truly evoke identical source waveforms, as our equality constraint does. Based on human psychophysical results [Previc, 1990; Skrandies, 1987], one would predict differences in response waveforms for upper and lower field stimuli [Lehmann and Skrandies, 1979; Portin et al., 1999; Skrandies, 1987]. It is

not clear if areas like V3 and VP, which respond to lower and upper field stimuli respectively, are even similar enough to be considered parts of the same visual area [Burkhalter and Van Essen, 1986; Felleman et al., 1997; Zeki, 2003]. The smoothness constraint we described does allow for possible differences between stimulus locations, but an alternative is to estimate waveforms separately for V3 and VP, or for upper and lower field stimuli for all visual areas.

Another significant simplification we made was to model each stimulus location for a given visual area with a single dipole, instead of, for example, modeling the spatial spread of the electrophysiological response. We presmoothed the normal vectors over the cortical surface, so this effectively used a Gaussian function to model the spatial spread. A more realistic approach would be to specify a patch of cortex based on receptive field sizes for each visual area. Alternatively, the shape of the fall-off could be estimated from the MEG/EEG data by optimizing weights of neighboring vertices surrounding the surface vertex chosen as the center of the receptive cortex. It may also be possible to estimate separate waveforms for center and surround, potentially resulting in a more accurate model and a better fit to the data.

### Technical Considerations Affecting Accuracy of Source Estimates

The first of several technical considerations potentially affecting the accuracy of source estimates concerns the validity of using fMRI to determine MEG/EEG source dipole locations. The most important question is whether signals localized with fMRI correspond to the generators of MEG/EEG signals. Simultaneous electrophysiological and hemodynamic measurements in animals have demonstrated that the differences in location of peak activation by the two measures is less than 1 mm [Devor et al., 2005; Grinvald et al., 1986; Thompson et al., 2003]. Possible nonlinearities between cortical current amplitudes and hemodynamic responses [Devor et al., 2003; Wager et al., 2005; Wan et al. 2006] are not a concern; because instead of relying on

**Figure 9.**

Insensitivity of estimated source waveform to typical errors in modeled dipole orientations with equality constraint. (**A**) Residual error of simulated source estimates with varying levels of average random dipole orientation errors (0, 18°, 30°, 37°, 41°, and 44°), corresponding to 0–5 vertex distance away from "true" dipole location. (**B**) Simulated source estimates with no dipole errors. (**C**) Simulated source estimates with 41° dipole errors, corresponding to ∼4 vertex displacement from "true" location. [Color figure can be viewed in the online issue, which is available at www.interscience.wiley.com.]

**Figure 10.**

Sensitivity of estimated source waveform to typical errors in modeled dipole orientations with independence between stimulus locations. (**A**) Residual error of simulated source estimates with varying levels of average random dipole orientation errors (0, 18°, 30°, 37°, 41°, and 44°), corresponding to 0–5 vertex distance away from "true" dipole location. (**B**) Simulated V1 source estimates with no dipole errors. (**C**) Simulated V1 source estimates with 41° dipole errors, corresponding to ∼4 vertex displacement from "true" location. [Color figure can be viewed in the online issue, which is available at www.interscience.wiley.com.]

fMRI signal amplitudes, we used the phase of periodic signals to select dipole locations. Similarly, the spatial spread of fMRI signals relative to electrophysiological measures is not an issue because fMRI was used only to select the center of the patch of cortex receptive to a particular stimulus location.

Assuming that it is valid to use MRI and fMRI data to create dipole models for MEG/EEG data, accurate registration between MRI, fMRI, and MEG/EEG data is important for constructing accurate dipole models. Besides finding the best fitting registration between fMRI and MRI or MEG/EEG and MRI, which we did through manual registration and visual inspection, there are a few other important issues that affect the accuracy of these registrations. First, gradient coil nonlinearities result in scanner-type specific image distortions in structural MRI images. Second, magnetic susceptibility inhomogeneities in the brain produce distortion in fMRI images. If uncorrected, it will be impossible to correctly register structural and functional MRI images and errors in the dipole model will be inevitable. We greatly reduced this source of error by correcting for these distortions (see Methods). Third, head motion during MEG acquisition would introduce errors in the MRI to MEG registration. Such motion could be prevented by using a subject-specific bite-bar or corrected offline if real-time head tracking were used.

Even with perfect co-registration of structural and functional MRI images, the accuracy of the dipole models remains limited by the spatial resolution of the fMRI images, physiological and scanner noise in the fMRI images, and the reliability of manually chosen dipole locations. We used voxels that were slightly larger than 3 mm isotropic, but smaller voxels (e.g. 2 mm isotropic) have been used effectively to provide higher resolution retinotopic maps [Kastner et al., 2007; Schira et al., 2007]. In addition, the selection of dipole locations could be automated, and hopefully improved, by fitting a retinotopic map template to the data using nonlinear optimization methods [Dougherty et al., 2003; Schira et al., 2007]. Improved spatial resolution of fMRI data and more reliable selection of dipole locations should provide more accurate dipole models; however, we found that even small displacements result in relatively large changes in dipole orientations. Thus, it is reassuring that constraining the solutions with multiple stimulus locations yielded source estimates less susceptible to random errors in the modeled dipole orientations than source waveforms estimated independently for each stimulus location. It is likely that increasing the number of stimulus locations included in the model, for example by sampling at multiple eccentricities, would further improve the robustness of the estimates.

The accuracy of the overall fit to the data is also limited by the accuracy of the forward model. We used the BEM, which uses realistic surfaces reconstructed from high-resolution MR images of the head. Because MEG is relatively insensitive to the conductivity profile of the head, BEM

models, or even spherical shell models, have been shown to result in low localization errors [Leahy et al., 1998]. In contrast, because the spatial spread of EEG signals is quite sensitive to the low conductivity in the skull, BEM models are a significant improvement over spherical shell models [Fuchs et al., 1998; Yvert et al., 1995; Zanow and Peters, 1995]. Source estimates using the finite element method (FEM) are more accurate, especially for EEG, although this method is computationally intensive and limited by the resolution of the MR images used to create the models [Gencer and Acar, 2004; Ollikainen et al., 1999; Wen and Li, 2006; Wolters et al., 2006]. Properties of sublayers of the skull, which affect the local conductivity, may be difficult to resolve with standard structural MR images and actual conductivity values for those sub-layers may be unknown.

## Potential Applications

In this manuscript we have described a new method that provides the means to noninvasively study the temporal properties of individual visual areas. This method offers the possibility of studying how the timing or magnitude of activation in multiple visual areas varies as a function of stimulus properties, attentional state, or task demands. For example, one could measure how the time courses of individual visual areas are modulated by stimulus contrast. Because visual areas such as V1 and V3 display differences in sensitivity to changes in stimulus contrast that are measurable with fMRI [Avidan et al., 2002; Buracas et al., 2005; Kastner et al., 2004; Tootell et al., 1995], this would test the sensitivity of the method to detect changes in response amplitude. Hemispheric or upper/lower visual field asymmetries can also be studied, as can interactions between early visual areas and higher-level visual and multi-sensory areas.

This method is also well suited to the study of the modulation of VERs by selective attention. MEG/EEG studies have demonstrated attentional modulation of the VER due to selective spatial attention [Di Russo et al., 2003; Martinez et al., 1999, 2001; Noesselt et al., 2002], but because ECD source analysis is unable to reliably distinguish between activity in the individual visual areas, a definitive analysis of the temporal patterns of attentional modulation requires source analysis methods that are able to confidently separate signals from multiple, simultaneously active, visual areas.

## REFERENCES

Ahlfors SP, Ilmoniemi RJ, Hamalainen MS (1992): Estimates of visually evoked cortical currents. Electroencephalogr Clin Neurophysiol 82:225–236.

Aine CJ, Supek S, George JS, Ranken D, Lewine J, Sanders J, Best E, Tiee W, Flynn ER, Wood CC (1996): Retinotopic organization of human visual cortex: Departures from the classical model. Cereb Cortex 6:354–361.

Aine C, Huang M, Stephen J, Christner R (2000): Multistart algorithms for MEG empirical data analysis reliably characterize locations and time courses of multiple sources. Neuroimage 12:159–172.

Avidan G, Harel M, Hendler T, Ben-Bashat D, Zohary E, Malach R (2002): Contrast sensitivity in human visual areas and its relationship to object recognition. J Neurophysiol 87:3102–3116.

Barth DS, Di S (1991): Laminar excitability cycles in neocortex. J Neurophysiol 65:891–898.

Brefczynski JA, DeYoe EA (1999): A physiological correlate of the 'spotlight' of visual attention. Nat Neurosci 2:370–374.

Bullier J, Nowak LG (1995): Parallel versus serial processing: New vistas on the distributed organization of the visual system. Curr Opin Neurobiol 5:497–503.

Buracas GT, Fine I, Boynton GM (2005): The relationship between task performance and functional magnetic resonance imaging response. J Neurosci 25:3023–3031.

Burkhalter A, Van Essen DC (1986): Processing of color, form and disparity information in visual areas VP and V2 of ventral extrastriate cortex in the macaque monkey. J Neurosci 6:2327–2351.

Butler SR, Georgiou GA, Glass A, Hancox RJ, Hopper JM, Smith KR (1987): Cortical generators of the CI component of the pattern-onset visual evoked potential. Electroencephalogr Clin Neurophysiol 68:256–267.

Chang H, Fitzpatrick JM (1992): A technique for accurate magnetic resonance imaging in the presenceof field inhomogeneities. IEEE Trans Med Imaging 11:319–329.

Chen WT, Ko YC, Liao KK, Hsieh JC, Yeh TC, Wu ZA, Ho LT, Lin YY (2005): Optimal check size and reversal rate to elicit pattern-reversal MEG responses. Can J Neurol Sci 32:218–224.

Clark VP, Fan S, Hillyard SA (1995): Identification of early visual evoked potential generators by retinotopic and topographic analyses. Hum Brain Mapp 2:170–187.

Colby CL, Goldberg ME (1999): Space and attention in parietal cortex. Annu Rev Neurosci 22:319–349.

Cox RW (1996): AFNI: Software for analysis and visualization of functional magnetic resonance neuroimages. Comput Biomed Res 29:162–173.

Creutzfeldt OD, Watanabe S, Lux HD (1966): Relations between EEG phenomena and potentials of single cortical cells. I. Evoked responses after thalamic and epricortical stimulation Electroencephalogr Clin Neurophysiol 20:1–18.

Dale AM, Sereno MI (1993): Improved localization of cortical activity by combining EEG and MEG with MRI cortical surface reconstruction: A linear approach. J Cogn Neurosci 5:162–176.

Dale AM, Halgren E (2001): Spatiotemporal mapping of brain activity by integration of multiple imaging modalities. Curr Opin Neurobiol 11:202–208.

Dale AM, Fischl B, Sereno MI (1999): Cortical surface-based analysis. I. Segmentation and surface reconstruction Neuroimage 9:179–194.

Dale AM, Liu AK, Fischl BR, Buckner RL, Belliveau JW, Lewine JD, Halgren E (2000): Dynamic statistical parametric mapping: Combining fMRI and MEG for high-resolution imaging of cortical activity. Neuron 26:55–67.

de Munck JC (1992): A linear discretization of the volume conductor boundary integral equation using analytically integrated elements. IEEE Trans Biomed Eng 39:986–990.

Devor A, Dunn AK, Andermann ML, Ulbert I, Boas DA, Dale AM (2003): Coupling of total hemoglobin concentration, oxygenation, and neural activity in rat somatosensory cortex. Neuron 39:353–359.

Devor A, Ulbert I, Dunn AK, Narayanan SN, Jones SR, Andermann ML, Boas DA, Dale AM (2005): Coupling of the cortical hemodynamic response to cortical and thalamic neuronal activity. Proc Natl Acad Sci USA 102:3822–3827.

DeYoe EA, Carman GJ, Bandettini P, Glickman S, Wieser J, Cox R, Miller D, Neitz J (1996): Mapping striate and extrastriate visual areas in human cerebral cortex. Proc Natl Acad Sci USA 93:2382–2386.

Di Russo F, Martinez A, Sereno MI, Pitzalis S, Hillyard SA (2001): Cortical sources of the early components of the visual evoked potential. Hum Brain Mapp 15:95–111.

Di Russo F, Martinez A, Hillyard SA (2003): Source analysis of event-related cortical activity during visuo-spatial attention. Cereb Cortex 13:486–499.

Di Russo F, Pitzalis S, Spitoni G, Aprile T, Patria F, Spinelli D, Hillyard SA (2005): Identification of the neural sources of the pattern-reversal VEP. Neuroimage 24:874–886.

Dougherty RF, Koch VM, Brewer AA, Fischer B, Modersitzki J, Wandell BA (2003): Visual field representations and locations of visual areas V1/2/3 in human visual cortex. J Vis 3:586–598.

Einevoll GT, Pettersen KH, Devor A, Ulbert I, Halgren E, Dale AM (2007): Laminar population analysis: Estimating firing rates and evoked synaptic activity from multielectrode recordings in rat barrel cortex. J Neurophysiol 97:2174–2190.

Engel SA, Rumelhart DE, Wandell BA, Lee AT, Glover GH, Chichilnisky EJ, Shadlen MN (1994): fMRI of human visual cortex. Nature 369:525.

Felleman DJ, Van Essen DC (1991): Distributed hierarchical processing in the primate cerebral cortex. Cereb Cortex 1:1–47.

Felleman DJ, Burkhalter A, Van Essen DC (1997): Cortical connections of areas V3 and VP of macaque monkey extrastriate visual cortex. J Comp Neurol 379:21–47.

Fischl B, Sereno MI, Dale AM (1999): Cortical surface-based analysis. II: Inflation, flattening, and a surface-based coordinate system. Neuroimage 9:195–207.

Fuchs M, Drenckhahn R, Wischmann HA, Wagner M (1998): An improved boundary element method for realistic volume-conductor modeling. IEEE Trans Biomed Eng 45:980–997.

Gandhi SP, Heeger DJ, Boynton GM (1999): Spatial attention affects brain activity in human primary visual cortex. Proc Natl Acad Sci USA 96:3314–3319.

Gardner JL, Sun P, Waggoner RA, Ueno K, Tanaka K, Cheng K (2005): Contrast adaptation and representation in human early visual cortex. Neuron 47:607–620.

Gencer NG, Acar CE (2004): Sensitivity of EEG and MEG measurements to tissue conductivity. Phys Med Biol 49:701–717.

Grinvald A, Lieke E, Frostig RD, Gilbert CD, Wiesel TN (1986): Functional architecture of cortex revealed by optical imaging of intrinsic signals. Nature 324:361–364.

Hagler DJ Jr, Sereno MI (2006): Spatial maps in frontal and prefrontal cortex. Neuroimage 29:567–577.

Hagler DJ Jr, Saygin AP, Sereno MI (2006): Smoothing and cluster thresholding for cortical surface-based group analysis of fMRI data. Neuroimage 33:1093–1103.

Hagler DJ Jr, Riecke L, Sereno MI (2007): Parietal and superior frontal visuospatial maps activated by pointing and saccades. Neuroimage 35:1562–1577.

Hamalainen M, Hari R, Ilmoniemi RJ, Knuutila J, Lounasmaa OV (1993): Magnetoencephalography—Theory, instrumentation, and applications to noninvasive studies of the working human brain. Rev Mod Phys 65:413–497.

Hoekema R, Wieneke GH, Leijten FS, van Veelen CW, van Rijen PC, Huiskamp GJ, Ansems J, van Huffelen AC (2003): Measurement of the conductivity of skull, temporarily removed during epilepsy surgery. Brain Topogr 16:29–38.

Huk AC, Dougherty RF, Heeger DJ (2002): Retinotopy and functional subdivision of human areas MT and MST. J Neurosci 22:7195–7205.

Jeffreys DA (1968): Separable components of human evoked responses to spatially patterned visual fields. Electroencephalogr Clin Neurophysiol 24:596.

Jeffreys DA, Axford JG (1972): Source locations of pattern-specific components of human visual evoked potentials. I. Component of striate cortical origin. Exp Brain Res 16:1–21.

Jeffreys DA, Smith AT (1979): The polarity inversion of scalp potentials evoked by upper and lower half-field stimulus patterns: Latency or surface distribution differences? Electroencephalogr Clin Neurophysiol 46:409–415.

Jovicich J, Czanner S, Greve D, Haley E, van der Kouwe A, Gollub R, Kennedy D, Schmitt F, Brown G, Macfall J, Fischi B, Dale A. (2006): Reliability in multi-site structural MRI studies: Effects of gradient non-linearity correction on phantom and human data. Neuroimage 30:436–443.

Kastner S, Ungerleider LG (2000): Mechanisms of visual attention in the human cortex. Annu Rev Neurosci 23:315–341.

Kastner S, O'Connor DH, Fukui MM, Fehd HM, Herwig U, Pinsk MA (2004): Functional imaging of the human lateral geniculate nucleus and pulvinar. J Neurophysiol 91:438–448.

Kastner S, DeSimone K, Konen CS, Szczepanski SM, Weiner KS, Schneider KA (2007): Topographic maps in human frontal cortex revealed in memory-guided saccade and spatial working-memory tasks. J Neurophysiol 97:3494–3507.

Leahy RM, Mosher JC, Spencer ME, Huang MX, Lewine JD (1998): A study of dipole localization accuracy for MEG and EEG using a human skull phantom. Electroencephalogr Clin Neurophysiol 107:159–173.

Lehmann D, Skrandies W (1979): Multichannel evoked potential fields show different properties of human upper and lower hemiretina systems. Exp Brain Res 35:151–159.

Liu AK, Belliveau JW, Dale AM (1998): Spatiotemporal imaging of human brain activity using functional MRI constrained magnetoencephalography data: Monte Carlo simulations. Proc Natl Acad Sci USA 95:8945–8950.

Liu AK, Dale AM, Belliveau JW (2002): Monte Carlo simulation studies of EEG and MEG localization accuracy. Hum Brain Mapp 16:47–62.

Mangun GR (1995): Neural mechanisms of visual selective attention. Psychophysiology 32:4–18.

Martinez A, Anllo-Vento L, Sereno MI, Frank LR, Buxton RB, Dubowitz DJ, Wong EC, Hinrichs H, Heinze HJ, Hillyard SA (1999): Involvement of striate and extrastriate visual cortical areas in spatial attention. Nat Neurosci 2:364–369.

Martinez A, DiRusso F, Anllo-Vento L, Sereno MI, Buxton RB, Hillyard SA (2001): Putting spatial attention on the map: Timing and localization of stimulus selection processes in striate and extrastriate visual areas. Vis Res 41:1437–1457.

Morgan PS, Bowtell RW, McIntyre DJ, Worthington BS (2004): Correction of spatial distortion in EPI due to inhomogeneous static magnetic fields using the reversed gradient method. J Magn Reson Imaging 19:499–507.

Mosher JC, Leahy RM, Lewis PS (1999): EEG and MEG: Forward solutions for inverse methods. IEEE Trans Biomed Eng 46:245–259.

Noesselt T, Hillyard SA, Woldorff MG, Schoenfeld A, Hagner T, Jancke L, Tempelmann C, Hinrichs H, Heinze HJ (2002): Delayed striate cortical activation during spatial attention. Neuron 35:575–587.

Ollikainen JO, Vauhkonen M, Karjalainen PA, Kaipio JP (1999): Effects of local skull inhomogeneities on EEG source estimation. Med Eng Phys 21:143–154.

Oostendorp TF, van Oosterom A (1989): Source parameter estimation in inhomogeneous volume conductors of arbitrary shape. IEEE Trans Biomed Eng 36:382–391.

Portin K, Vanni S, Virsu V, Hari R (1999): Stronger occipital cortical activation to lower than upper visual field stimuli. Neuromagnetic recordings. Exp Brain Res 124:287–294.

Previc FH (1990): Functional specialization in the upper and lower visual fields in humans: Its ecological origins and neurophysiological implications. Behav Brain Sci 13:519–575.

Raiguel SE, Lagae L, Gulyas B, Orban GA (1989): Response latencies of visual cells in macaque areas V1, V2 and V5. Brain Res 493:155–159.

Reinsberg SA, Doran SJ, Charles-Edwards EM, Leach MO (2005): A complete distortion correction for MR images: II. Rectification of static-field inhomogeneities by similarity-based profile mapping. Phys Med Biol 50:2651–2661.

Sasaki Y, Hadjikhani N, Fischl B, Liu AK, Marrett S, Dale AM, Tootell RB (2001): Local and global attention are mapped retinotopically in human occipital cortex. Proc Natl Acad Sci USA 98:2077–2082.

Scherg M.1990.Fundamentals of dipole source analysis. In:Grandori F, Hoke MLRG, editors. Auditory Evoked Magnetic Fields and Electric Potentials. Basel: Karger. pp 40–69.

Schira MM, Wade AR, Tyler CW (2007): Two-dimensional mapping of the central and parafoveal visual field to human visual cortex. J Neurophysiol 97:4284–4295.

Schluppeck D, Glimcher P, Heeger DJ (2005): Topographic organization for delayed saccades in human posterior parietal cortex. J Neurophysiol 94:1372–1384.

Schmidt DM, George JS, Wood CC (1999): Bayesian inference applied to the electromagnetic inverse problem. Hum Brain Mapp 7:195–212.

Schmolesky MT, Wang Y, Hanes DP, Thompson KG, Leutgeb S, Schall JD, Leventhal AG (1998): Signal timing across the macaque visual system. J Neurophysiol 79:3272–3278.

Schroeder CE, Tenke CE, Givre SJ, Arezzo JC, Vaughan HG Jr (1991): Striate cortical contribution to the surface-recorded pattern-reversal VEP in the alert monkey. Vis Res 31:1143–1157.

Schroeder CE, Mehta AD, Givre SJ (1998): A spatiotemporal profile of visual system activation revealed by current source density analysis in the awake macaque. Cereb Cortex 8:575–592.

Seiffert AE, Somers DC, Dale AM, Tootell RB (2003): Functional MRI studies of human visual motion perception: texture, luminance, attention and after-effects. Cereb Cortex 13:340–349.

Sereno MI (1998): Brain mapping in animals and humans. Curr Opin Neurobiol 8:188–194.

Sereno MI, Allman JM.1991.Cortical visual areas in mammals. In:Leventhal A, editor. The Neural Basis of Visual Function. London: Macmillan. pp 160–172.

Sereno MI, McDonald CT, Allman JM (1994): Analysis of retinotopic maps in extrastriate cortex. Cereb Cortex 4:601–620.

Sereno MI, Dale AM, Reppas JB, Kwong KK, Belliveau JW, Brady TJ, Rosen BR, Tootell RB (1995): Borders of multiple visual areas in humans revealed by functional magnetic resonance imaging. Science 268:889–893.

Sereno MI, Pitzalis S, Martinez A (2001): Mapping of contralateral space in retinotopic coordinates by a parietal cortical area in humans. Science 294:1350–1354.

Sharon D, Hamalainen MS, Tootell RB, Halgren E, Belliveau JW (2007): The advantage of combining MEG and EEG: Comparison to fMRI in focally stimulated visual cortex. Neuroimage 36:1225–1235.

Silver MA, Ress D, Heeger DJ (2005): Topographic maps of visual spatial attention in human parietal cortex. J Neurophysiol 94:1358–1371.

Singh KD, Smith AT, Greenlee MW (2000): Spatiotemporal frequency and direction sensitivities of human visual areas measured using fMRI. Neuroimage 12:550–564.

Skrandies W.1987.The upper and lower visual field of man: Electrophysiological and functional differences. In:Ottoson D, editor. Progress in Sensory Physiology. Berlin: Springer. pp 1–93.

Slotnick SD, Klein SA, Carney T, Sutter E, Dastmalchi S (1999): Using multi-stimulus VEP source localization to obtain a retinotopic map of human primary visual cortex. Clin Neurophysiol 110:1793–1800.

Slotnick SD, Schwarzbach J, Yantis S (2003): Attentional inhibition of visual processing in human striate and extrastriate cortex. Neuroimage 19:1602–1611.

Somers DC, Dale AM, Seiffert AE, Tootell RB (1999): Functional MRI reveals spatially specific attentional modulation in human primary visual cortex. Proc Natl Acad Sci USA 96:1663–1668.

Supek S, Aine CJ (1993): Simulation studies of multiple dipole neuromagnetic source localization: model order and limits of source resolution. IEEE Trans Biomed Eng 40:529–540.

Swisher JD, Halko MA, Merabet LB, McMains SA, Somers DC (2007): Visual topography of human intraparietal sulcus. J Neurosci 27:5326–5337.

Thompson JK, Peterson MR, Freeman RD (2003): Single-neuron activity and tissue oxygenation in the cerebral cortex. Science 299:1070–1072.

Tootell RB, Reppas JB, Kwong KK, Malach R, Born RT, Brady TJ, Rosen BR, Belliveau JW (1995): Functional analysis of human MT and related visual cortical areas using magnetic resonance imaging. J Neurosci 15:3215–3230.

Tootell RB, Mendola JD, Hadjikhani NK, Ledden PJ, Liu AK, Reppas JB, Sereno MI, Dale AM (1997): Functional analysis of V3A and related areas in human visual cortex. J Neurosci 17:7060–7078.

Tootell RB, Hadjikhani N, Hall EK, Marrett S, Vanduffel W, Vaughan JT, Dale AM (1998a): The retinotopy of visual spatial attention. Neuron 21:1409–1422.

Tootell RB, Hadjikhani NK, Vanduffel W, Liu AK, Mendola JD, Sereno MI, Dale AM (1998b): Functional analysis of primary visual cortex (V1) in humans. Proc Natl Acad Sci USA 95:811–817.

Vanni S, Warnking J, Dojat M, Delon-Martin C, Bullier J, Segebarth C (2004): Sequence of pattern onset responses in the human visual areas: An fMRI constrained VEP source analysis. Neuroimage 21:801–817.

Wager TD, Vazquez A, Hernandez L, Noll DC (2005): Accounting for nonlinear BOLD effects in fMRI: Parameter estimates and a model for prediction in rapid event-related studies. Neuroimage 25:206–218.

Wan X, Riera J, Iwata K, Takahashi M, Wakabayashi T, Kawashima R (2006): The neural basis of the hemodynamic response nonlinearity in human primary visual cortex: Implications for neurovascular coupling mechanism. Neuroimage 32:616–625.

Ward BD (2000): Deconvolution Analysis of FMRI Time Series Data. AFNI 3dDeconvolve Documentation. Medical College of Wisconsin: Wisconsin.

Wen P, Li Y (2006): EEG human head modelling based on heterogeneous tissue conductivity. Aust Phys Eng Sci Med 29:235–240.

Wolters CH, Anwander A, Tricoche X, Weinstein D, Koch MA, MacLeod RS (2006): Influence of tissue conductivity anisotropy on EEG/MEG field and return current computation in a realistic head model: A simulation and visualization study using high-resolution finite element modeling. Neuroimage 30:813–826.

Yvert B, Bertrand O, Echallier JF, Pernier J (1995): Improved forward EEG calculations using local mesh refinement of realistic head geometries. Electroencephalogr Clin Neurophysiol 95: 381–392.

Zanow F, Peters MJ (1995): Individually shaped volume conductor models of the head in EEG source localisation. Med Biol Eng Comput 33:582–588.

Zeki S (2003): Improbable areas in the visual brain. Trends Neurosci 26:23–26.